



## Nonequilibrium plastic roughening of metallic glasses yields self-affine topographies with strain-rate and temperature-dependent scaling exponents

Wolfram G. Nöhring <sup>1,2</sup> Adam R. Hinkle <sup>3,4</sup> and Lars Pastewka <sup>1,3,5</sup>

<sup>1</sup>Department of Microsystems Engineering, University of Freiburg, 79110 Freiburg, Germany

<sup>2</sup>Max-Planck Institute for Chemical Energy Conversion, 45470 Mülheim an der Ruhr, Germany

<sup>3</sup>Institute for Applied Materials, Karlsruhe Institute of Technology, 76131 Karlsruhe, Germany

<sup>4</sup>DCS Corporation, Belcamp, Maryland 21017, USA

<sup>5</sup>Cluster of Excellence livMatS, Freiburg Center for Interactive Materials and Bioinspired Technologies, University of Freiburg, 79110 Freiburg, Germany



(Received 11 January 2022; accepted 6 July 2022; published 21 July 2022)

We study nonequilibrium roughening during compressive plastic flow of initially flat Cu<sub>50</sub>Zr<sub>50</sub> metallic glass using large-scale molecular dynamics simulations. Roughness emerges at atomically flat interfaces beyond the yield point of the glass. A self-affine rough topography is imprinted at yield and is reinforced during subsequent deformation. The imprinted topographies have Hurst exponents that decrease with increasing strain rate and temperature. After yield, the root-mean-square roughness amplitude grows as the square root of the applied strain with a prefactor that also drops with increasing strain rate and temperature. Our calculations reveal the emergence of spatial power-law correlations from homogeneous samples during plastic flow with exponents that depend on the rate of deformation and the temperature. The results have implications for interpreting and engineering roughness profiles.

DOI: [10.1103/PhysRevMaterials.6.075603](https://doi.org/10.1103/PhysRevMaterials.6.075603)

### I. INTRODUCTION

Roughness controls many interfacial phenomena. The most prominent examples are arguably the influence of roughness on friction [1,2], adhesion [3–8], and electric [9] and thermal [10] transport. It is therefore useful to characterize surface roughness, and to understand the mechanisms that produce it, including growth, erosion, and fracture. Here, we focus on plastic deformation as a roughening mechanism: When a solid deforms irreversibly because of external forces, a signature of the deformation process is imprinted on the surface. For example, crystal dislocations in metals [11–15] or shear bands and fractures in rocks [16] leave slip traces behind that roughen surfaces.

Unlike crystalline materials, the fundamental deformation event in glasses is not a slip trace but a localized shear transformation or STZ (shear transformation zone) [17–20]. At low temperature (or slow deformation), these can coalesce to form deformation avalanches that potentially span the size of the whole system [21,22]. Despite the importance of glasses for engineering applications and the wide interest in deformation of glasses in physics, little is known about the nonequilibrium processes forming their surface morphology.

Glasses formed by quenching have surfaces that are well described by capillary waves [23–25]. However, many natural and industrially processed surfaces, including those of noncrystalline materials, are found to be self-affine fractals with power-law scaling of heights [26–31]. The root-mean-square (rms) amplitude of surface height fluctuations  $h_{\text{rms}}(L)$  measured in a square region with sides of length  $L$ , then scales as  $h_{\text{rms}}(L) \propto L^H$  where  $H$  is the Hurst exponent.

Recent simulation studies have shown that deformation is one possible origin of self-affinity. For example, Milanese *et al.* [32] have observed self-affine roughening in 2D discrete-element simulations of sliding contacts that formed abrasive third bodies. We recently used molecular dynamics calculations to show that self-affine roughness emerges naturally during compression of atomically flat surfaces made from pure metals, crystalline alloys, and metallic glasses [15]. Similar results have been obtained by Vacher and de Wijn for the surface of polymers [33].

We here present evidence that—unlike in crystalline materials [15]—the roughness characteristics of a glass depend strongly on temperature and deformation rate. We show that two regimes of temperature and strain rate must be distinguished. In quasistatic deformation, and at the lowest temperatures and rates, the topography is dominated by system-spanning shear bands. Self-affine scaling of surface heights is nevertheless plausible through a mechanism similar to slip of crystal dislocations, but with a shear band as the fundamental slip event. Higher temperatures and strain rates lead to the formation of smoother and more diffuse topographies that exhibit self-affine scaling at small scales. Their rms roughness  $h_{\text{rms}}$  grows roughly as  $h_{\text{rms}} \propto \varepsilon^{1/2}$  at large strain.

Published by the American Physical Society under the terms of the [Creative Commons Attribution 4.0 International](https://creativecommons.org/licenses/by/4.0/) license. Further distribution of this work must maintain attribution to the author(s) and the published article's title, journal citation, and DOI.

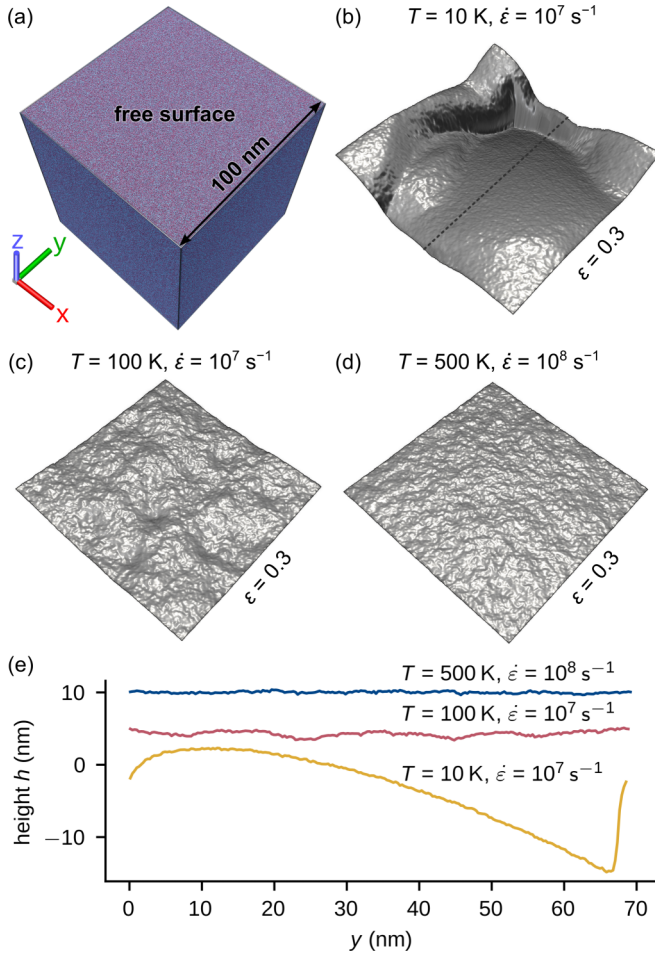


FIG. 1. (a)  $\text{Cu}_{50}\text{Zr}_{50}$  cube with a side length of 100 nm and a free surface in the  $z$  direction. We simulated biaxial compression along the  $x$  and  $y$  directions. (b) Topography of the surface after 30% compression with a rate of  $10^7 \text{ s}^{-1}$  at 10 K. A shear band has formed. No such distinct feature is visible at (c) 100 K and (d) 500 K. The topography becomes smoother with increasing temperature. (e) Line scans along the  $y$  direction extracted from the topographies shown in [(b)–(d)]. The starting point is approximately the midpoint along the  $x$  direction. The dashed line in (b) shows the approximate position of the scans. The curves for  $T = 100 \text{ K}$  and  $T = 500 \text{ K}$  have been shifted up by 5 nm and 10 nm, respectively, for better visibility.

Our simulations show that the topography is imprinted shortly after yield and is reinforced during subsequent deformation.

## II. METHODS

To study the emergence of surface roughness, we simulated  $100 \times 100 \times 100 \text{ nm}^3$  cubes of amorphous  $\text{Cu}_{50}\text{Zr}_{50}$  using molecular dynamics. The initial configuration shown in Fig. 1(a), contained  $5.8 \times 10^7$  atoms, interacting with the embedded atom method potential [34] of Cheng and Ma [35]. The initial structure was melt-quenched at a rate of  $10^{11} \text{ Ks}^{-1}$ , followed by equilibration for 100 ps at the target temperature and zero pressure. The systems were fully periodic during quench and equilibration, after which we opened the boundaries along the  $z$  direction, creating two free surfaces. The

samples were equilibrated for 100 ps after creating the free surfaces and before compression.

We compressed these samples by dynamically reducing the lengths of the simulation cell in the  $x$  and  $y$  directions. The rate of compression was equal in both directions. We report results in terms of the applied engineering strain  $\varepsilon(t) = 1 - L(t)/L_0$ , where  $L(t)$  is the linear length of the cell (at time  $t$ ), and  $L_0$  the initial initial length. Since a jump in the strain rate generates undesirable shock waves, we gradually increased  $\dot{\varepsilon}(t)$  from zero to a constant value during the first 100 ps of the simulation. We carried out simulations at final strain rates of  $10^7 \text{ s}^{-1}$  and  $10^8 \text{ s}^{-1}$ .

During deformation, we controlled the temperature using a dissipative particle dynamics (DPD) [36] thermostat with a cutoff radius of  $6.5 \text{ \AA}$ —equal to the cutoff radius of the potential—and a damping parameter  $\gamma = 5 \times 10^{-3} \text{ eVps/\AA}^2$ , which leads to a characteristic damping time of approximately 1 ps. Unlike Langevin or Nosé-Hoover thermostats, the Gallilean-invariant DPD thermostat does not overdamp long-wavelength modes, which is important for large-scale simulations such as those reported here.

Plastic deformation roughened the initially flat sample surfaces, which we quantified from a pixel representation  $h_{xy}(\varepsilon)$  of the topography with lateral pixel size  $L_{\text{pix}} \approx 0.3 \text{ nm}$ .  $h_{xy}$  is the height of the topmost atom (bottommost for bottom surface) associated with the pixel with center coordinates  $x$  and  $y$ . A pixel size of 0.3 nm is small enough to resolve short-wavelength components of the topography and large enough to avoid artifacts when assigning heights; see Appendix. We performed all statistical analysis on  $h_{xy}$ , e.g., the root-mean-square roughness  $h_{\text{rms}} = \langle h_{xy}^2 \rangle$  where  $\langle \cdot \rangle$  is the average over all pixels. We assume that the mean of each height map is zero,  $\langle h_{xy} \rangle = 0$ .

## III. RESULTS

Figures 1(b)–1(d) show  $h_{xy}$  after 30% compression in our dynamic tests. At the lowest rate and temperature ( $10^7 \text{ s}^{-1}$  and 10 K, Fig. 1(b), the most prominent feature is a lentil-shaped dip formed by shear bands. We find a similar topography in a quasistatic simulation (not shown), where we imposed compressive strain on the cell in increments of  $\Delta\varepsilon = 10^{-4}$  by affinely remapping all coordinates, followed by subsequent relaxation down to a force of  $10^{-3} \text{ eV\AA}^{-1}$  using the FIRE algorithm [37]. In the other simulations at higher temperature or higher rate, deformation was less localized and the resulting surface topography is more diffuse; see Figs. 1(c) and 1(d). The roughness amplitude generally decreases with increasing temperature and rate. At  $T = 500 \text{ K}$  and  $\dot{\varepsilon} = 10^8 \text{ s}^{-1}$ , the height range is only 2 nm. Figure 1(e) shows line scans along the  $y$  direction, extracted approximately at the midpoint of the edge along the  $x$  direction. The dashed line in Fig. 1(b) indicates the position of the scans.

Figure 2(a) shows the mean lateral stress  $(\sigma_{xx} + \sigma_{yy})/2$  as a function of strain  $\varepsilon$ . In most cases, the purely linearly elastic regime does not end abruptly. After the peak, the stress decreases smoothly, as expected [38–40], and stabilizes at the steady-state flow stress. Increasing temperature and decreasing rate lowers the peak and flow stresses. The only exceptions are the two simulations with shear banding: the quasistatic test

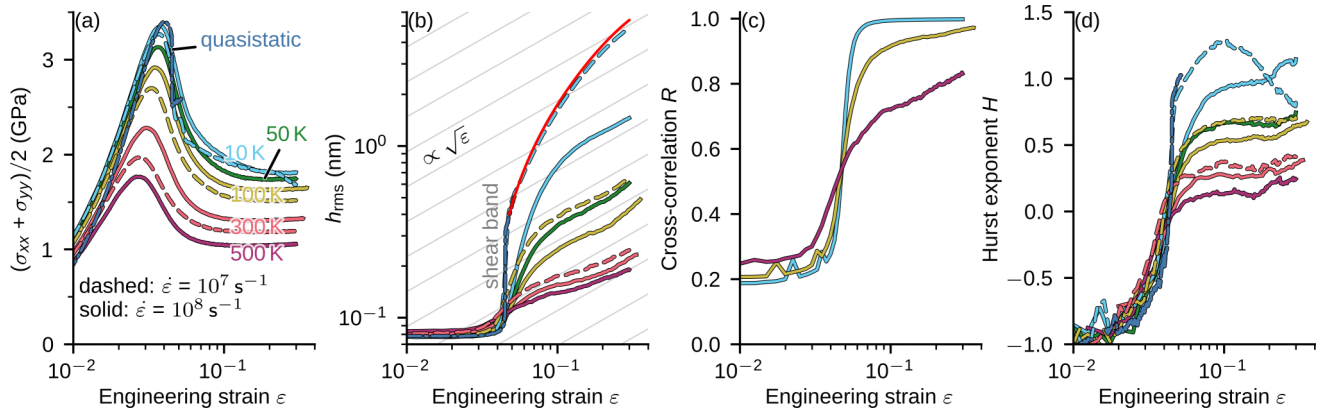


FIG. 2. (a) Lateral normal stress vs compressive strain  $\varepsilon$  in simulations with different strain rates  $\dot{\varepsilon}$  and temperatures  $T$ . (b) Root-mean-square roughness  $h_{\text{rms}}$ , which increases after yield. A shear band forms in the quasistatic simulation, and in low-rate, low-temperature simulations (here  $\dot{\varepsilon} = 10^7 \text{ s}^{-1}$  at 10 K). The thin-red line is a model of  $h_{\text{rms}}$  for a topography dominated by a shear band (see text). (c) Cross correlation  $R$  (see text) between subsequent topographies at intervals of  $\Delta\varepsilon \approx 0.0025$ . (d) Hurst exponent extracted from fits to the PSD (see text).

and the dynamic simulation with  $\dot{\varepsilon} = 10^7 \text{ s}^{-1}$  at 10 K. In the former case, a sharp stress drop is visible. In the latter case, the stress decreases again close to  $\varepsilon = 0.3$ .

In all cases,  $h_{\text{rms}}$  [see Fig. 2(b)] is initially less than 0.1 nm, as should be expected for an atomically flat surface, but increases after peak stress. The rate of roughening depends on  $\dot{\varepsilon}$  and  $T$ . The steepest increase in  $h_{\text{rms}}$  is seen in the quasistatic simulation and the simulation with  $\dot{\varepsilon} = 10^7 \text{ s}^{-1}$  at 10 K. Increasing  $\dot{\varepsilon}$  and  $T$  leads to a more gradual transition, and lower  $h_{\text{rms}}$  at the same strain. At the highest temperatures, there is little difference between the curves for 300 K and 500 K. At large strain,  $h_{\text{rms}} \propto \varepsilon^\alpha$  with  $\alpha \approx 0.5$ , except in the simulation with  $\dot{\varepsilon} = 10^7 \text{ s}^{-1}$  at 10 K that forms a shear band.

While  $h_{\text{rms}}$  increases continuously, there is little qualitative difference between the topography formed during yield, and the topography at later stages of deformation. To quantify this observation, we calculated the cross correlation  $R(\varepsilon) = \langle h_{xy}(\varepsilon - \Delta\varepsilon)h_{xy}(\varepsilon) / [h_{\text{rms}}(\varepsilon - \Delta\varepsilon)h_{\text{rms}}(\varepsilon)] \rangle^{1/2}$  between subsequent simulation snapshots with  $\Delta\varepsilon = 0.0025$  for the simulations with  $\dot{\varepsilon} = 10^8 \text{ s}^{-1}$  [Fig. 2(c)]. Before yield, the cross correlation is small ( $\approx 0.2$ ), indicating that there are not many common features between subsequent snapshots. This is not surprising, since  $h_{\text{rms}}$  is so low that the structural disorder of the glassy state dominates the topography. After the peak stress, the cross correlation increases significantly, with the strongest and most rapid increase seen in the simulation at the lowest temperature of  $T = 10 \text{ K}$ . In this case, the cross correlation jumps to a value close to one, indicating that the topography is reinforced—peaks grow higher and valleys become deeper—with little qualitative change. Increasing temperature reduces the correlation, but beyond  $\varepsilon \approx 0.04$ , it stays above 0.5.

In order to examine lateral correlations in the topography, we compute the power spectral density (PSD),  $C_{q_x q_y}^{2D} = L^{-2} |\hat{h}_{q_x q_y}|^2$  (or rather its radial average  $C_q^{\text{iso}}$ ), where  $\hat{h}_{q_x q_y}$  is the discrete Fourier transform of  $h_{xy}$ . (See Ref. [41] for the conventions used here.) If the topography is self-affine with Hurst exponent  $H$ , then the PSD scales as  $C_q^{\text{iso}} \propto q^{-2-2H}$ .

Figure 3(a) shows how  $C_q^{\text{iso}}$  evolves with strain  $\varepsilon$ . The PSD is constant at small strain, where the residual roughness is given by uncorrelated quenched disorder of the glassy state. At yield,  $C_q^{\text{iso}}$  begins to grow, as can be seen in the curve for  $\varepsilon = 0.04$ , which is just past the peak stress in this simulation. Topographic structure emerges first at small  $q$  or long wavelengths. At a large strain of  $\varepsilon = 0.3$ ,  $C_q^{\text{iso}}$  has a linear region in the double-logarithmic plot, which is the signature of self-affine (scale-free) roughness.

Figure 3(b) shows  $C_q^{\text{iso}}$  from the simulations at 100 K, 300 K at  $\varepsilon = 0.3$ . In the double-logarithmic plot, all curves have a linear region at intermediate  $q$ . As a guide to the eye,

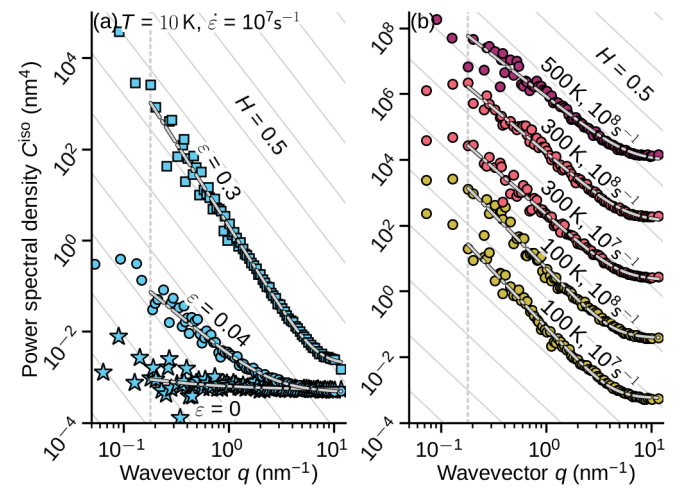


FIG. 3. (a) Radially averaged power spectral density (PSD)  $C_q^{\text{iso}}$  of the surface heights, at three different strains in the simulation with  $T = 10 \text{ K}$  and  $\dot{\varepsilon} = 10^7 \text{ s}^{-1}$ . As a consequence of plastic deformation,  $C_q^{\text{iso}}$  increases with strain  $\varepsilon$ , first at long wavelengths (small wavevectors  $q$ ). Despite a shear band that forms in this simulation,  $C_q^{\text{iso}}$  is approximately linear in the double logarithmic plot at large  $\varepsilon$ . (b)  $C_q^{\text{iso}}$  at  $\varepsilon = 0.3$  in simulations at and above 100 K. Gray lines: Fit to a white noise plus power-law model  $C_q^{\text{iso}} = C_{\text{wn}} + C_{\text{pl}} q^{-2-2H}$  in the region  $q > 0.18 \text{ nm}^{-1}$ m; the cutoff is indicated by a vertical-dashed line. The ordinates in (b) have been shifted for better visibility.

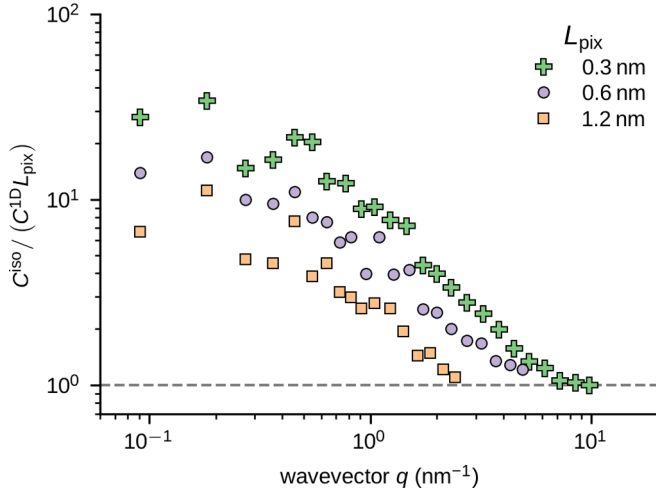


FIG. 4. Ratio of the isotropic and the one-dimensional power spectral densities  $C_q^{\text{iso}}$  and  $C_q^{\text{1D}}$ , respectively, normalized by pixel size  $L_{\text{pix}}$ , for three different pixel sizes. At large wavevectors, all curves approach unity, indicating that they are controlled by white noise in this limit. Data is computed at  $\varepsilon = 0.3$  from the simulation with rate  $\dot{\varepsilon} = 10^7 \text{ s}^{-1}$  at temperature  $T = 100 \text{ K}$ .

the gray lines in Figs. 3(a) and 3(b) show ideal fractal scaling with a Hurst exponent  $H = 0.5$ . We extract an estimate for the Hurst exponent from these calculations by fitting the simple model  $C_q^{\text{iso}} = C_{\text{wn}} + C_f q^{-2-2H}$  to the PSD data, excluding data in the long wavelength region  $q < 0.18 \text{ nm}^{-1}$ . The constant  $C_{\text{wn}}$  is a white noise contribution and  $C_f$  is the amplitude of the fractal regime.

The individual fits are shown as dashed-gray lines in Figs. 3(a) and 3(b). The combination of white noise and a self-affine regime describes the data well, even at  $\varepsilon = 0.04$  in Fig. 3(a) where roughening has just begun. The fits now allow us to plot the evolution of  $H$  with strain  $\varepsilon$  [Fig. 2(d)]. There is an initial region of negative  $H$  where the surfaces are flat and do not show self-affine scaling, followed by a jump to a finite value as the surfaces yield.  $H$  depends on temperature and strain rate, with lower temperatures and lower strain rates leading to larger values of  $H$ .

We now show in more detail that the tail of the PSD at large wavevectors in Fig. 3 is indeed white noise, using a method described in Ref. [41]. The *isotropic* PSD  $C_q^{\text{iso}}$  is the radial average of the full two-dimensional power spectral density map  $C_{q_x q_y}^{\text{2D}}$ . White noise with a standard deviation  $\sigma_{\text{wn}}$  generates a contribution  $C_{\text{wn}}^{\text{iso}} = L_{\text{pix}}^2 \sigma_{\text{wn}}^2$ , where  $L_{\text{pix}}$  is the linear dimension of the (square) pixel. We can also interpret  $h_{xy}$  as a series of line scans and calculate their average one-dimensional PSD,  $C_q^{\text{1D}}$ . Here, white noise makes a contribution  $C_{\text{wn}}^{\text{iso}} = L_{\text{pix}} \sigma_{\text{wn}}^2$ . Thus, the ratio of  $C_q^{\text{iso}}$  and  $C_q^{\text{1D}}$  will contain a term  $C_q^{\text{iso}}/C_q^{\text{1D}} = L_{\text{pix}}$ . If the PSD is indeed controlled by white noise, then  $C_q^{\text{iso}}/(L_{\text{pix}} C_q^{\text{1D}}) \rightarrow 1$  at large wavelengths.

We computed this ratio for the configuration with  $\varepsilon = 0.3$  from the simulation with rate  $\dot{\varepsilon} = 10^7 \text{ s}^{-1}$  at temperature  $T = 100 \text{ K}$ . Figure 4 shows the ratio for three different pixel sizes. All curves approach a value of unity at large wavevectors,

which is the signature of white noise. This means while self-affinity emerges at large wavelength, the quenched disorder of the glass determines the structure at small wavelengths.

#### IV. DISCUSSION

At low temperature ( $T = 10 \text{ K}$ ) and strain rate ( $\dot{\varepsilon} = 10^7 \text{ s}^{-1}$ ), the system is near the athermal quasistatic (or overdamped) regime of deformation [42], with the quasistatic simulation as the limiting case. In line with many previous investigations [43,44], we observe system-spanning shear bands. Considering the high strain rates that are typical for molecular calculations, it is perhaps surprising that we can approach the quasistatic limit with our dynamic simulations. In what follows, we invoke a model by Hentschel *et al.* [22] to show that system-spanning shear bands, the characteristic feature in both simulations, can be expected almost up to a rate of  $\dot{\varepsilon} = 10^7 \text{ s}^{-1}$ , at least at zero temperature.

Hentschel *et al.* argued that there is a critical cutoff scale  $\xi$  for the size of a deformation avalanche that depends on shear rate. (Related observations on such a cutoff have been made in other papers [21,45].) For a system with free boundaries, this corresponds to the size up to which percolation of system-spanning shear bands occurs. For  $L > \xi$ , many uncorrelated plastic events will occur simultaneously, suppressing the formation of a shear band.  $\xi$  depends on the deformation rate and arises due to a competition between the elastic relaxation time and the characteristic time between plastic events. It is given by

$$\frac{\xi}{\langle \lambda \rangle} = \left[ \left( \frac{\bar{\varepsilon}}{\sigma_y \langle \lambda \rangle^d} \right) \left( \frac{c}{\langle \lambda \rangle \dot{\varepsilon}} \right) \right]^{1/(1-\beta d)}, \quad (1)$$

where  $\langle \lambda \rangle$  is the mean interatomic distance,  $\sigma_y$  the flow stress,  $\bar{\varepsilon}$  the mean potential energy drop per atom during a plastic event,  $c$  the speed of sound,  $d$  the dimension, and  $\beta$  the exponent of the power-law relation between average stress drop and number of atoms.

We have estimated  $\xi$  for our case. By fitting Hooke's law to stress-strain curves from deformation tests carried out with smaller ( $L \approx 10 \text{ nm}$ ) cubes that were prepared with the same quench rate, we obtain  $C_{44} = 23.8 \text{ GPa}$  at  $T = 100 \text{ K}$ . At the same temperature, the larger configuration used in the simulations reported in the main text has an initial side length of  $L = 98.6 \text{ nm}$  and a density of  $7228.9 \text{ kg/m}^3$ . This gives a speed of sound in the transversal direction of  $c = \sqrt{C_{44}/\rho} = 1815.6 \text{ ms}^{-1}$ . From the peak of the radial distribution function, we estimate  $\langle \lambda \rangle = 0.28 \text{ nm}$  for Cu-Zr bonds. Our estimate of  $\sigma_y$  is based on the average lateral normal stress  $\sigma = (\sigma_{xx} + \sigma_{yy})/2$  in the region  $0.2 \leq \varepsilon \leq 0.3$ ; see Fig. 2(a). We take for  $\sigma_y$  the corresponding shear stress on planes inclined  $45^\circ$  to the  $z$  direction. For a stress tensor with nonzero components  $\sigma_{xx}$ ,  $\sigma_{yy}$ , and  $\sigma_{xy}$ ,  $\sigma_y = (\sigma_{xx} + \sigma_{yy})/4$ . At  $\dot{\varepsilon} = 10^8 \text{ s}^{-1}$  and  $T = 100 \text{ K}$ , we obtain  $\sigma_y = 0.82 \text{ GPa}$ .

The mean potential energy drop per atom  $\bar{\varepsilon}$  is the parameter that is most difficult to estimate. We cannot directly compute this average from our data, because we cannot resolve all events with the given strain increment or rate. However, we recorded the potential energy per atom, and this allows an approximation. On average, an atom will move from a

high-energy to a low-energy position, thus we assume  $\bar{\epsilon} \propto \bar{\sigma}_U$ , where  $\bar{\sigma}_U$  is the average of the standard deviations  $\sigma_{U,Cu}$  and  $\sigma_{U,Zr}$  of the potential energy of Cu and Zr atoms, respectively,  $\bar{\sigma}_U = [(\sigma_{U,Cu}^2 + \sigma_{U,Zr}^2)/2]^{1/2}$ . We obtain  $\bar{\epsilon} = \sqrt{2}\sigma_U$  as the standard deviation of the difference of two random variables with standard deviation  $\sigma_U$ . From the configuration at  $\epsilon = 0.3$  in the simulation with  $\dot{\epsilon} = 10^8 \text{ s}^{-1}$  and  $T = 100 \text{ K}$ , we obtain  $\bar{\epsilon} = 0.17 \text{ eV}$ . Our simulations are three dimensional, hence  $d = 3$ . Finally, we use  $\beta = \alpha - 1$ , where  $\alpha$  is the exponent of the power law relating the average potential energy drop to the number of atoms [22]. From Fig. 2 in Ref. [46] we obtain  $\alpha \approx 0.53$ , giving  $\beta = -0.47$  or the scaling relationship  $\xi \propto \dot{\epsilon}^{-0.41}$ . We note that this exponent appears to be consistent with the characteristic correlation length between plastic flow events for binary Lennard-Jones glasses reported in Ref. [47],  $\xi \propto \dot{\epsilon}^{-0.4}$  in 2D and  $\xi \propto \dot{\epsilon}^{-0.3}$  in 3D.

Using this data, we find  $L = \xi$  at  $\dot{\epsilon} = 7.2 \times 10^6 \text{ s}^{-1}$ , not far from the minimum strain rate  $10^7 \text{ s}^{-1}$  considered in this paper. Thus, our observation of system-spanning shear bands at the lowest rate is consistent with theory. Both our data and the model indicate that a dynamic simulation can approximate the quasistatic regime, even at the comparatively high strain rates used in molecular dynamics simulations. We note that Hentschel *et al.* [22] propose another cutoff length scale, where temperature fluctuations suppress avalanches. However, using our data for this estimate predicts that all our simulations should be free of shear bands, which is clearly not the case.

We turn to the effect of shear bands on the topography, which is formed by the steps left of the surface. The corresponding  $h_{\text{rms}}$  curve in Fig. 2(b) can thus be understood using a simple model of the growth of a single surface step described by the function  $h(x) = a(x - L(\epsilon)/2)$ , where  $a$  is the slope of the step. The mean height is zero, hence the  $h_{\text{rms}} = L^{-1} \int_0^L h^2(x) dx = aL/\sqrt{12}$ . The length decreases with strain as  $L(\epsilon) = (1 - \epsilon)L_0$ . We assume that the slope is a linear function of strain, i.e.,  $a(\epsilon) = A(\epsilon - \epsilon_b) + B$ , where  $A$  and  $B$  are constants, and  $\epsilon_b$  is the strain at which the band is formed. In reality, the band forms over a range of strain. However, this range is narrow, as can be seen in Fig. 2(b), where  $\epsilon_b \approx 4.8 \times 10^{-2}$  is a good approximation. At  $\epsilon_b$ ,  $h_{\text{rms}}$  jumps to a base value  $h_{\text{rms}}(\epsilon_b) \equiv h_b \approx 4 \text{ nm}$ , which determines  $B$ . By substituting  $L(\epsilon_b)$  and  $a(\epsilon_b)$  into the formula for  $h_{\text{rms}}$ , we obtain  $B = h_b \sqrt{12}/[(1 - \epsilon_b)L_0]$ , hence

$$h_{\text{rms}}(\epsilon) = \frac{L_0}{\sqrt{12}} \left( A(\epsilon - \epsilon_b) + \frac{h_b \sqrt{12}}{(1 - \epsilon_b)L_0} \right) (1 - \epsilon). \quad (2)$$

With  $A = 1$ , we obtain the red curve in Fig. 2(b), which is close to the data for  $\dot{\epsilon} = 10^7 \text{ s}^{-1}$  and  $T = 10 \text{ K}$ .

It is remarkable that the topography appears to be self-affine at large strain [Fig. 3(a)], even though the overall topography is dominated by a single system-spanning shear band. We note that an idealized sawtooth profile (that is *not* self-affine) also exhibits power-law scaling  $C_q^{\text{iso}} \propto q^{-3}$  of the power spectral density—however, with a smaller apparent Hurst exponent of  $H = 0.5$ , while our fit of the data in Fig. 3(a) yields  $H = 0.8$ . (Note that a random distribution of multiple such steps leads to a self-affine topography, albeit

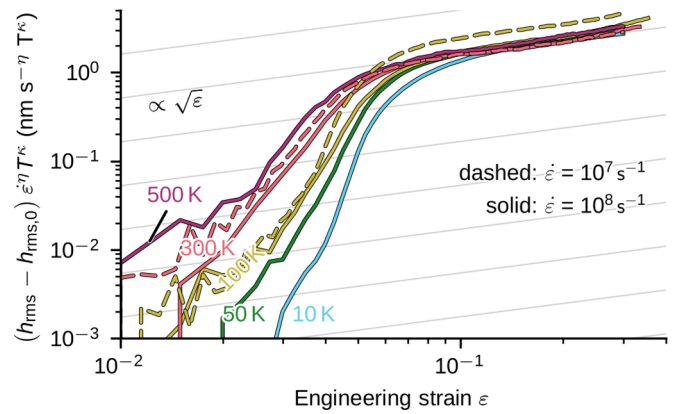


FIG. 5. Root-mean-square roughness  $h_{\text{rms}}$ , divided by  $\dot{\epsilon}^{-\eta} T^{-\kappa}$ , with  $\eta = 0.1$  and  $\kappa = 0.7$ . This normalization collapses the  $h_{\text{rms}}$  curves at high strain.

at scales larger than our simulations—see also the discussion on dislocations, that leave behind atomic-scale steps, in Ref. [15].) Since power-law scaling of  $C_q^{\text{iso}}$  is also plausible in the other simulations with higher rates and temperatures, where no system-spanning shear bands are formed, these shear bands likely do not control the exponent of  $C_q^{\text{iso}}$  in Fig. 3(a).

Decreasing either rate or temperature increases both  $h_{\text{rms}}$  and  $H$ . In this respect, the glass is different from metal crystals, where  $h_{\text{rms}}$  and  $H$  due to roughening by plastic deformation are independent of rate and temperature [15]. We note in particular that the dependence of the scaling exponent  $H$  on rate and temperature is unusual, as scaling exponents in power-law correlated data of phase transitions or critical phenomena are widely regarded as universal [48]. These observations touch upon an ongoing discussion whether the yielding transition (in glassy materials) can be strictly regarded as a phase transition [49–53], that becomes “rounded” at finite temperature [54,55]. In our calculations, this rounding is manifested in the transition from a sharp drop in stress at low temperature over a range of strains in Fig. 2(a). Conversely, the Hurst exponent does *not* appear to “round”; it jumps to a finite value at the yielding transition even at high temperature [Fig. 2(d)]. This indicates a sharp transition, albeit towards a temperature-dependent (and hence nonuniversal) exponent of the spatial correlations.

Finally, we attempt an empirical scaling collapse of our data for the characteristic length in our system, the height amplitude  $h_{\text{rms}}$ . We attempt to collapse the  $h_{\text{rms}}(\epsilon)$  curves from those simulations where no system-spanning shear band is nucleated assuming the empirical relation  $h_{\text{rms}} \propto \dot{\epsilon}^{-\eta} T^{-\kappa}$ . Before dividing by  $\dot{\epsilon}^{-\eta} T^{-\kappa}$ , we subtracted the small baseline roughness  $h_{\text{rms},0}$  of the undeformed state that reflects the white noise contribution to surface roughness, which we do not expect to scale. We computed  $h_{\text{rms},0}$  as the mean value of  $h_{\text{rms}}(\epsilon)$  for  $\epsilon < 0.01$ . Figure 5 shows the curves after normalization with  $\eta = 0.1$  and  $\kappa = 0.7$ . This choice collapses the data beyond the yield point ( $\epsilon \gtrsim 0.1$ ).

We note that the exponent  $\eta$  is obviously different from the exponent governing the length scale  $\zeta$ . This indicates that the mechanism that determines the nucleation of a system-spanning shear band is different from the

deformation mechanism underlying the roughening. We believe that roughening is determined by the rate-dependence of single shear transformation events, which is weaker than the rate dependence of their percolation.

## V. SUMMARY AND CONCLUSIONS

In summary, the evolution of the surface roughness of a deformed  $\text{Cu}_{50}\text{Zr}_{50}$  metallic glass reflects the dependence of plastic flow on rate  $\dot{\epsilon}$  and temperature  $T$ . At low values of these parameters, the topography is dominated by system-spanning shear bands. At higher temperatures and rates, a more diffuse topography emerges, with some traces of universality: At large strain, the root-mean-square roughness tends to grow roughly as  $h_{\text{rms}} \propto \epsilon^\alpha$ , with  $\alpha \approx 0.5$ . Moreover,  $h_{\text{rms}} \propto \dot{\epsilon}^{-\eta} T^{-\kappa}$  at large strain with  $\eta \approx 0.1$  and  $\kappa \approx 0.7$ . Regardless of rate and temperature, the power spectral density of all surfaces can be described as the superposition of a self-affine part and constant noise from quenched, glassy disorder.

Our results remain valid for small-scale roughness of systems with evolving shear bands. We note that similar to dislocations [12,15], a network of shear bands forms a network of steps on a surface, which also carries the signature of self-affine scaling with an exponent that depends on the lateral correlation of these steps. This indicates that during the formation of real-world surfaces, a number of mechanisms may be active at different scales that all lead to self-affine geometries.

## ACKNOWLEDGMENTS

We thank J. Griebner, R. Leute, G. Moras, L. Ponson, and M. Zaiser for useful discussion. We used LAMMPS [56] for all calculations and OVITO PRO [57] and PYVISTA [58] for postprocessing and visualization. Topography data was analyzed with CONTACT.ENGINEERING [59]. We acknowledge support from the European Research Council (Grant No. StG-757343) and the Deutsche Forschungsgemeinschaft (Grant No. PA 2023/2). Calculations were carried out at the Jülich Supercomputing Center (JUWELS, Grant No. hka18) and postprocessed at the University of Freiburg (NEMO, Deutsche Forschungsgemeinschaft Grant No. INST 39/963-1 FUGG). Data is stored on bwSFS (University of Freiburg, Deutsche Forschungsgemeinschaft Grant No. INST 39/1099-1 FUGG).

## APPENDIX: EFFECT OF PIXEL SIZE

To check the effect of pixel size, we recalculated  $h_{\text{rms}}$  and  $C_q^{\text{iso}}$  with different pixel sizes  $L_{\text{pix}}$  for the configuration at  $\epsilon = 0.3$  from the simulation with  $\dot{\epsilon} = 10^7 \text{ s}^{-1}$  and  $T = 100 \text{ K}$ . Figure 6(a) shows  $h_{\text{rms}}$  as a function of  $L_{\text{pix}}$ . The dotted line indicates our default value  $L_{\text{pix}} = 0.3 \text{ nm}$ . Below this value,

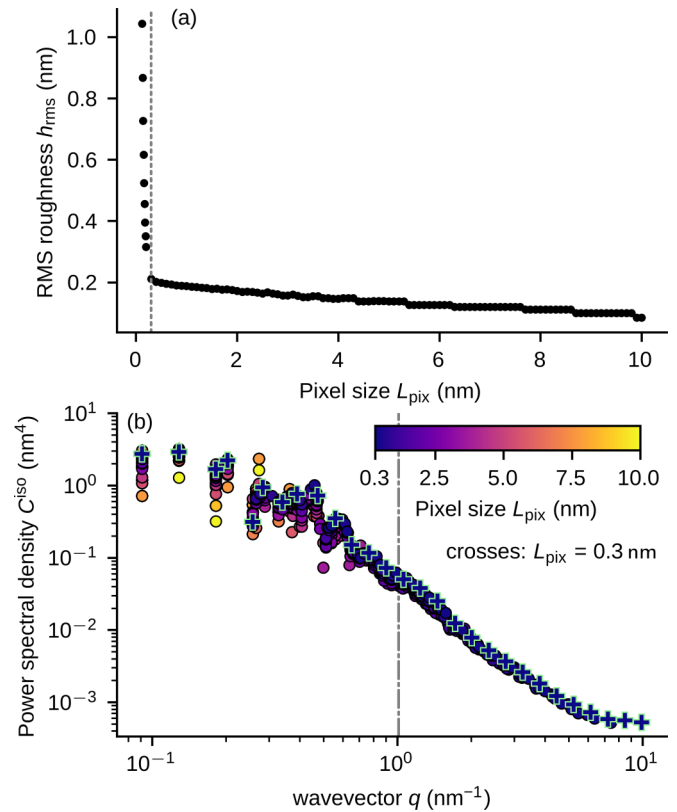


FIG. 6. (a) RMS roughness  $h_{\text{rms}}$  as a function of pixel size  $L_{\text{pix}}$ . The dotted line indicates the value 0.3 nm used in the calculations reported in the main text. For smaller values of  $L_{\text{pix}}$   $h_{\text{rms}}$  increases rapidly because the algorithm for assigning heights to pixels fails. (b) Power spectral density  $C_q^{\text{iso}}$  for different values of  $L_{\text{pix}} \geq 0.3 \text{ nm}$ . The different curves collapse, however the long-wavevector cutoff decreases. The dash-dotted line shows the maximum wavevector at  $L_{\text{pix}} = 3 \text{ nm}$ .

$h_{\text{rms}}$  increases rapidly with decreasing  $L_{\text{pix}}$ . Here, our algorithm for assigning heights to pixels fails. Pixels are so small that some do not cover any surface atoms, only atoms in the bulk, resulting in artificially inflated height differences. Below 0.12 nm, some pixels do not cover any atoms at all. For  $L_{\text{pix}} \geq 3 \text{ nm}$ ,  $h_{\text{rms}}$  decreases with increasing  $L_{\text{pix}}$ . Between  $L_{\text{pix}} = 0.3 \text{ nm}$  and  $L_{\text{pix}} = 3 \text{ nm}$ ,  $h_{\text{rms}}$  decreases by 25%.

Figure 6(b) shows  $C_q^{\text{iso}}$  for different values of  $L_{\text{pix}} \geq 0.3 \text{ nm}$ . The curves collapse, but the cutoff at large wavevectors decreases with increasing  $L_{\text{pix}}$ . The dash-dotted line indicates the largest wavevector for  $L_{\text{pix}} = 3 \text{ nm}$ . We conclude that  $L_{\text{pix}} = 0.3 \text{ nm}$  is large enough to avoid artifacts of our pixelization algorithm, and small enough to observe linear scaling of  $C_q^{\text{iso}}$  in the log-log plot.

- [1] M. Urbakh, J. Klafter, D. Gourdon, and J. N. Israelachvili, The nonlinear nature of friction, *Nature (London)* **430**, 525 (2004).  
 [2] B. N. J. Persson, O. Albohr, U. Tartaglino, A. I. Volokitin, and E. Tosatti, On the nature of surface roughness with application

to contact mechanics, sealing, rubber friction and adhesion, *J. Phys.: Condens. Matter* **17**, R1 (2005).

- [3] K. N. G. Fuller and D. Tabor, The effect of surface roughness on the adhesion of elastic solids, *Proc. R. Soc. London A* **345**, 327 (1975).

- [4] D. Maugis, On the contact and adhesion of rough surfaces, *J. Adhes. Sci. Technol.* **10**, 161 (1996).
- [5] B. N. J. Persson and E. Tosatti, The effect of surface roughness on the adhesion of elastic solids, *J. Chem. Phys.* **115**, 5597 (2001).
- [6] B. N. J. Persson, Adhesion between Elastic Bodies with Randomly Rough Surfaces, *Phys. Rev. Lett.* **89**, 245502 (2002).
- [7] L. Pastewka and M. O. Robbins, Contact between rough surfaces and a criterion for macroscopic adhesion, *Proc. Natl. Acad. Sci. USA* **111**, 3298 (2014).
- [8] S. Dalvi, A. Gujrati, S. R. Khanal, L. Pastewka, A. Dhinojwala, and T. D. B. Jacobs, Linking energy loss in soft adhesion to surface roughness, *Proc. Natl. Acad. Sci. USA* **116**, 25484 (2019).
- [9] L. Binder, Der Widerstand von Kontakten, *Elektrotechnik und Maschinenbau* **30**, 781 (1912).
- [10] B. Gotsmann and M. A. Lantz, Quantized thermal transport across contacts of rough surfaces, *Nat. Mater.* **12**, 59 (2013).
- [11] Y. Miura, Punched-out dislocation rosettes in low-dislocation-density copper, *J. Appl. Phys.* **43**, 2917 (1972).
- [12] M. Zaiser, F. M. Gasset, V. Koutsos, and E. C. Aifantis, Self-Affine Surface Morphology of Plastically Deformed Metals, *Phys. Rev. Lett.* **93**, 195507 (2004).
- [13] J. Gagel, D. Weygand, and P. Gumbsch, Formation of extended prismatic dislocation structures under indentation, *Acta Mater.* **111**, 399 (2016).
- [14] J. Gagel, D. Weygand, and P. Gumbsch, Discrete dislocation dynamics simulations of dislocation transport during sliding, *Acta Mater.* **156**, 215 (2018).
- [15] A. R. Hinkle, W. G. Nöhring, R. Leute, T. Junge, and L. Pastewka, The emergence of small-scale self-affine surface roughness from deformation, *Sci. Adv.* **6**, eaax0847 (2020).
- [16] H. Fossen, *Structural Geology*, 2nd ed. (Cambridge University Press, Cambridge, 2016).
- [17] F. Spaepen, A microscopic mechanism for steady state inhomogeneous flow in metallic glasses, *Acta Metall.* **25**, 407 (1977).
- [18] A. S. Argon, Plastic deformation in metallic glasses, *Acta Metall.* **27**, 47 (1979).
- [19] M. L. Falk and J. S. Langer, Dynamics of viscoplastic deformation in amorphous solids, *Phys. Rev. E* **57**, 7192 (1998).
- [20] T. C. Hufnagel, C. A. Schuh, and M. L. Falk, Deformation of metallic glasses: Recent developments in theory, simulations, and experiments, *Acta Mater.* **109**, 375 (2016).
- [21] A. Anaël and C. Caroli, Rate-Dependent Avalanche Size in Athermally Sheared Amorphous Solids, *Phys. Rev. Lett.* **103**, 065501 (2009).
- [22] H. G. E. Hentschel, S. Karmakar, E. Lerner, and I. Procaccia, Size of Plastic Events in Strained Amorphous Solids at Finite Temperatures, *Phys. Rev. Lett.* **104**, 025501 (2010).
- [23] J. Jackle and K. Kawasaki, Intrinsic roughness of glass surfaces, *J. Phys.: Condens. Matter* **7**, 4351 (1995).
- [24] T. Sarlat, A. Lelarge, E. Søndergård, and D. Vandembroucq, Frozen capillary waves on glass surfaces: An AFM study, *Eur. Phys. J. B* **54**, 121 (2006).
- [25] Z. Zhang, S. Ispas, and W. Kob, Roughness and Scaling Properties of Oxide Glass Surfaces at the Nanoscale, *Phys. Rev. Lett.* **126**, 066101 (2021).
- [26] R. S. Sayles and T. R. Thomas, Surface topography as a nonstationary random process, *Nature (London)* **271**, 431 (1978).
- [27] B. B. Mandelbrot, *The Fractal Geometry of Nature* (W. H. Freeman, San Francisco, 1982).
- [28] J. J. Mecholsky, D. E. Passoja, and K. S. Feinberg-Ringel, Quantitative analysis of brittle fracture surfaces using fractal geometry, *J. Am. Ceram. Soc.* **72**, 60 (1989).
- [29] D. Bonamy, L. Ponson, S. Prades, E. Bouchaud, and C. Guillot, Scaling Exponents for Fracture Surfaces in Homogeneous Glass and Glassy Ceramics, *Phys. Rev. Lett.* **97**, 135504 (2006).
- [30] T. Candela, F. Renard, Y. Klinger, K. Mair, J. Schmittbuhl, and E. E. Brodsky, Roughness of fault surfaces over nine decades of length scales, *J. Geophys. Res. - Solid Earth* **117**, B08409 (2012).
- [31] A. Gujrati, S. R. Khanal, L. Pastewka, and T. D. B. Jacobs, Combining TEM, AFM, and profilometry for quantitative topography characterization across all scales, *ACS Appl. Mater. Interfaces* **10**, 29169 (2018).
- [32] E. Milanese, T. Brink, R. Aghababaei, and J.-F. Molinari, Emergence of self-affine surfaces during adhesive wear, *Nat. Commun.* **10**, 1116 (2019).
- [33] R. Vacher and A. S. de Wijn, Molecular-dynamics simulations of the emergence of surface roughness in a polymer under compression, *Materials* **14**, 7327 (2021).
- [34] M. H. Müser, S. V. Sukhomlinov, and L. Pastewka, Interatomic potentials: Achievements and challenges, [arXiv:2204.09563](https://arxiv.org/abs/2204.09563) [Adv. Phys. X (to be published)].
- [35] Y. Q. Cheng and E. Ma, Atomic-level structure and structure-property relationship in metallic glasses, *Prog. Mater. Sci.* **56**, 379 (2011).
- [36] T. Soddemann, B. Dunweg, and K. Kremer, Dissipative particle dynamics: A useful thermostat for equilibrium and nonequilibrium molecular dynamics simulations, *Phys. Rev. E* **68**, 046702 (2003).
- [37] E. Bitzek, P. Koskinen, F. Gähler, M. Moseler, and P. Gumbsch, Structural Relaxation Made Simple, *Phys. Rev. Lett.* **97**, 170201 (2006).
- [38] J. Rottler and M. O. Robbins, Shear yielding of amorphous glassy solids: Effect of temperature and strain rate, *Phys. Rev. E* **68**, 011507 (2003).
- [39] R. Bhowmick, R. Raghavan, K. Chattopadhyay, and U. Ramamurty, Plastic flow softening in a bulk metallic glass, *Acta Mater.* **54**, 4221 (2006).
- [40] F. Shimizu, S. Ogata, and J. Li, Yield point of metallic glass, *Acta Mater.* **54**, 4293 (2006).
- [41] T. D. B. Jacobs, T. Junge, and L. Pastewka, Quantitative characterization of surface topography using spectral analysis, *Surf. Topogr.: Metrol. Prop.* **5**, 013001 (2017).
- [42] K. M. Salerno, C. E. Maloney, and M. O. Robbins, Avalanches in Strained Amorphous Solids: Does Inertia Destroy Critical Behavior?, *Phys. Rev. Lett.* **109**, 105703 (2012).
- [43] K. Albe, Y. Ritter, and D. Şopu, Enhancing the plasticity of metallic glasses: Shear band formation, nanocomposites and nanoglasses investigated by molecular dynamics simulations, *Mech. Mater.* **67**, 94 (2013).
- [44] M. Singh, M. Ozawa, and L. Berthier, Brittle yielding of amorphous solids at finite shear rates, *Phys. Rev. Materials* **4**, 025603 (2020).
- [45] C. Liu, E. E. Ferrero, F. Puosi, J.-L. Barrat, and K. Martens, Driving Rate Dependence of Avalanche Statistics and Shapes at the Yielding Transition, *Phys. Rev. Lett.* **116**, 065501 (2016).

- [46] N. P. Bailey, J. Schjøtz, A. Lemaître, and K. W. Jacobsen, Avalanche Size Scaling in Sheared Three-Dimensional Amorphous Solid, *Phys. Rev. Lett.* **98**, 095501 (2007).
- [47] J. T. Clemmer, K. M. Salerno, and M. O. Robbins, Criticality in sheared, disordered solids. I. Rate effects in stress and diffusion, *Phys. Rev. E* **103**, 042605 (2021).
- [48] H. E. Stanley, Scaling, universality, and renormalization: Three pillars of modern critical phenomena, *Rev. Mod. Phys.* **71**, S358 (1999).
- [49] P. K. Jaiswal, I. Procaccia, C. Rainone, and M. Singh, Mechanical Yield in Amorphous Solids: A First-Order Phase Transition, *Phys. Rev. Lett.* **116**, 085501 (2016).
- [50] G. Parisi, I. Procaccia, C. Rainone, and M. Singh, Shear bands as manifestation of a criticality in yielding amorphous solids, *Proc. Natl. Acad. Sci. USA* **114**, 5577 (2017).
- [51] M. Ozawa, L. Berthier, G. Biroli, A. Rosso, and G. Tarjus, Random critical point separates brittle and ductile yielding transitions in amorphous materials, *Proc. Natl. Acad. Sci. USA* **115**, 6656 (2018).
- [52] R. Jana and L. Pastewka, Correlations of non-affine displacements in metallic glasses through the yield transition, *J. Phys. Mater.* **2**, 045006 (2019).
- [53] M. Ozawa, L. Berthier, G. Biroli, and G. Tarjus, Role of fluctuations in the yielding transition of two-dimensional glasses, *Phys. Rev. Research* **2**, 023203 (2020).
- [54] E. E. Ferrero, A. B. Kolton, and E. A. Jagla, Yielding of amorphous solids at finite temperatures, *Phys. Rev. Materials* **5**, 115602 (2021).
- [55] M. Popović, T. W. J. de Geus, W. Ji, and M. Wyart, Thermally activated flow in models of amorphous solids, *Phys. Rev. E* **104**, 025010 (2021).
- [56] S. Plimpton, Fast parallel algorithms for short-range molecular dynamics, *J. Comput. Phys.* **117**, 1 (1995).
- [57] A. Stukowski, Visualization and analysis of atomistic simulation data with OVITO—The open visualization tool, *Modell. Simul. Mater. Sci. Eng.* **18**, 015012 (2010).
- [58] C. B. Sullivan and A. Kaszynski, PyVista: 3D plotting and mesh analysis through a streamlined interface for the visualization toolkit (VTK), *J. Open Source Softw.* **4**, 1450 (2019).
- [59] M. C. Röttger, A. Sanner, L. A. Thimons, T. Junge, A. Gujrati, J. M. Monti, W. G. Nöhning, T. D. B. Jacobs, and L. Pastewka, contact.engineering—Create, analyze and publish digital surface twins from topography measurements across many scales, [arXiv:2203.13606](https://arxiv.org/abs/2203.13606) [Surf. Topogr. Metrol. Prop. (to be published)].